Geochimica et Cosmochimica Acta 390 (2025) 251–263

Contents lists available at ScienceDirect

Geochimica et Cosmochimica Acta

journal homepage: www.elsevier.com/locate/gca

Fluid-mineral titanium isotope fractionation: Computational and empirical results with implications for mineral deposits

Christopher Emproto [a], Ryan Mathur [b], Mingguang Sun [c,*], Adam C. Simon [a], Linda Godfrey [d]

[a] University of Michigan, Ann Arbor, MI, USA
[b] Juniata College, Huntingdon, PA, USA
[c] Institute of Mineral Resources, Chinese Academy of Geological Sciences, Beijing, China
[d] Rutgers University, New Brunswick, NJ, USA

ARTICLE INFO

Associate editor: Marc Blanchard

Keywords:
Ti isotope fractionation
First principles molecular dynamics
Isotope geochemistry
Mineral deposits
Magnetite

ABSTRACT

Titanium (Ti) typically exhibits low mobility in geologic fluids due to the low aqueous solubility of common (Fe-) Ti oxide minerals. Consequently, Ti isotope variations ($\delta^{49/47}$Ti, given as δ^{49}Ti) in geologic systems are primarily attributed to magmatic differentiation. Thus, the potential for fluid-mineral fractionation has received less attention. However, ligand-rich fluids are capable of mobilizing Ti as observed in natural systems and laboratory studies. As hydrothermal ore mineralization is commonly associated with ligand-rich brines capable of transporting significant quantities of metals, Ti isotopes may aid in understanding mineralization and alteration in complex hydrothermal systems. Here we present data from computational modeling of various Ti coordination complexes theorized to exist in geologic systems and/or under relevant experimental conditions as well as computed fractionation factors for various Ti-bearing crystalline phases to investigate the basic mechanics of equilibrium fluid-mineral Ti isotope fractionation. These results indicate that equilibrium fluid-mineral Ti isotope exchange between our modeled Ti complexes and phases with 6-coordinated Ti is predicted to generally lead to enrichment of heavy Ti isotopes in the fluid. Because minerals with 6-coordinated Ti (such as magnetite and ilmenite) are the most important reservoirs of Ti in the solid Earth, Ti isotope equilibration between terrestrial rocks and fluids can be generalized to enrich the fluid in heavy Ti isotopes. We also performed magnetite-ülvospinel leaching experiments to investigate fluid-mineral Ti isotope fractionation in this phase. Mineral leaching experiments varying acid strength, leaching temperature, and reaction time with HCl and HF qualitatively support the prediction that the fluid phase will become enriched in heavy Ti isotopes during fluid-mineral interactions that approach equilibrium with Ti-rich magnetite. Additionally, the leaching data also suggest that the fluid becomes slightly enriched in lighter Ti isotopes when Ti exchange is limited—potentially due to kinetic effects. Therefore, magnetite from natural systems may be depleted in heavy Ti isotopes during regenerative mineral replacement involving equilibration with fluids or may possibly become depleted in light Ti isotopes under a kinetic fractionation regime—leading to mineral δ^{49}Ti values that are insufficiently explained by magmatic differentiation or inter-mineral fractionation. These results are a first look at fluid-mineral interactions that may affect Ti isotope fractionation in hydrothermal mineral systems, and Ti isotopes should be further studied as a potential method of understanding aqueous metal transport and tracing alteration in mineral deposits.

1. Introduction

Titanium (Ti) has five stable isotopes (^{46}Ti, ^{47}Ti, ^{48}Ti, ^{49}Ti, and ^{50}Ti) and is the ninth most abundant element in the Earth's crust—where Ti-rich minerals are ubiquitous and occur in every major rock type. Common Ti-bearing phases such as rutile, ilmenite, and magnetite are physically and chemically resilient minerals that often crystallize early in magmas and persist during metamorphism and weathering. These qualities have given Ti a reputation as immobile during the alteration and recycling of Earth materials (Van Baalen, 1993). Consequently, the potential for Ti isotope fractionation to occur during post- and non-magmatic processes such as hydrothermal alteration has received

* Corresponding author.
E-mail address: m.g.sun1990@pku.edu.cn (M. Sun).

https://doi.org/10.1016/j.gca.2024.12.007
Received 2 November 2023; Accepted 6 December 2024
Available online 15 December 2024

limited attention.

Terrestrial Ti isotope fractionation is primarily attributed to magmatic differentiation during which early forming Ti-bearing minerals preferentially incorporate light Ti isotopes, leaving the residual melt enriched in heavy Ti isotopes (Millet et al., 2016; Deng et al., 2019; Johnson et al., 2019; Hoare et al., 2020; Zhao et al., 2020). In silicate melts, Ti may be in 4-, 5-, or 6-fold coordination whereas Ti in common oxide minerals is chiefly in 6-fold sites (Farges et al., 1996; Farges and Brown, 1997). For oxide minerals with Ti in 6-fold coordinated crystallographic sites, it is more energetically favorable during crystal growth to incorporate Ti from the melt that is already in 6-fold coordination rather than requiring modification of 5-fold and 4-fold coordinated Ti complexes. As light Ti isotopes prefer larger coordination numbers (CNs), they are overrepresented among 6-fold coordinated Ti complexes relative to heavier Ti isotopes. As a result, common oxide minerals like (titano)magnetite, ilmenite, and rutile are predicted to become enriched in light Ti isotopes during growth in a silicate melt (Millet et al., 2016). As the average Ti CN of a silicate melt is inversely related to the melt's SiO_2 concentration (specifically, the bridging to non-bridging O ratio that increases with melt SiO_2), the extent of mass-dependent stable isotope fractionation between the melt and precipitating minerals increases with increasing SiO_2 and is therefore not solely a function of temperature (Millet et al., 2016; Deng et al., 2019; Zhao et al., 2020; Aarons et al., 2021). The mineral fractionation factor is further influenced by the abundance of Ti in the mineral, based upon computational modeling and investigations of natural systems (Hoare et al., 2020; Wang et al., 2020). The equilibrium fractionation behavior between a mineral and a melt is therefore a dynamic interplay between mineral composition, melt chemistry, and temperature.

The Ti isotope compositions of igneous rocks are strongly influenced by their differentiation histories. Meteorites, the bulk silicate Earth, ultramafic, and mafic materials primarily fall within a relatively narrow range of Ti isotope compositions spanning c. 0–0.3‰, reported as $\delta^{49/47}$Ti (given as δ^{49}Ti) relative to the Origins Laboratory Ti metal standard (OL-Ti; Millet et al., 2016) (Fig. 1). The much larger range of c. 0–2.0‰ δ^{49}Ti exhibited by more Si-rich rocks is explained by the compounding effects of removal of early-formed oxides, increasing melt polymerization, and decreasing liquidus temperatures (Millet et al., 2016; Aarons et al., 2021). Partial melting is not thought to be an important source of Ti isotope fractionation in igneous rocks (Millet et al., 2016; Deng et al., 2018).

Natural igneous magnetites with δ^{49}Ti values greater than that of the bulk melt are unlikely because the δ^{49}Ti difference between melt and magnetite in equilibrium ($\Delta^{49}Ti_{melt\text{-}magnetite}$) is greater than zero at magmatic temperatures (see Fig. S1). As a result, igneous magnetite would be isotopically lighter than the melt it crystallized from. This difference increases at lower temperatures and higher SiO_2 concentrations (corresponding to an increasing bridging to non-bridging O ratio; Millet et al., 2016; Zhao et al., 2020; Hoare et al., 2022). Thus, while felsic melts are interpreted to generally be isotopically heavier than mafic melts, there is a larger difference between a felsic melt and its Ti-rich oxide precipitates than that of a mafic melt (Millet et al., 2016; Hoare et al., 2022). Zhao et al. (2020) notes that magnetite favors light Ti isotopes more than other Ti-rich minerals including ilmenite, rutile, and pseudobrookite. Because these minerals all favor light Ti isotopes relative to a typical silicate melt, usually form early in its crystallization history, and would also contain the bulk of its Ti budget, magnetite would generally be expected to be isotopically lighter than the bulk melt/rock. Therefore, because the maximum δ^{49}Ti values of bulk igneous rocks are c. 2‰ (only three whole-rock samples exceed 2‰; Deng et al., 2019; Hoare et al., 2020), typical igneous magnetite δ^{49}Ti values are not expected to exceed c. 2‰. Very careful investigations of igneous systems have facilitated the construction of models to predict magmatic Ti isotope fractionation for different magma types (e.g., Aarons et al., 2020, 2021). However, these models are not applicable to fluid-mediated systems.

Millet et al. (2016) broadly interpreted Ti isotope signatures as unresponsive to hydrothermal fluids based upon analyses of eclogites and serpentinites and found δ^{49}Ti values consistent with their source materials, reinforcing prior assumptions about Ti mobility (Ryzhenko et al., 2006). Additionally, He et al. (2022) estimated minor (c. 0.2‰) fluid-mineral Ti isotope fractionation during extensive lateritic weathering of basaltic rock. Aarons et al. (2023) also noted minor (up to c. 0.1‰) Ti isotope fractionation during intense chemical weathering in soils.

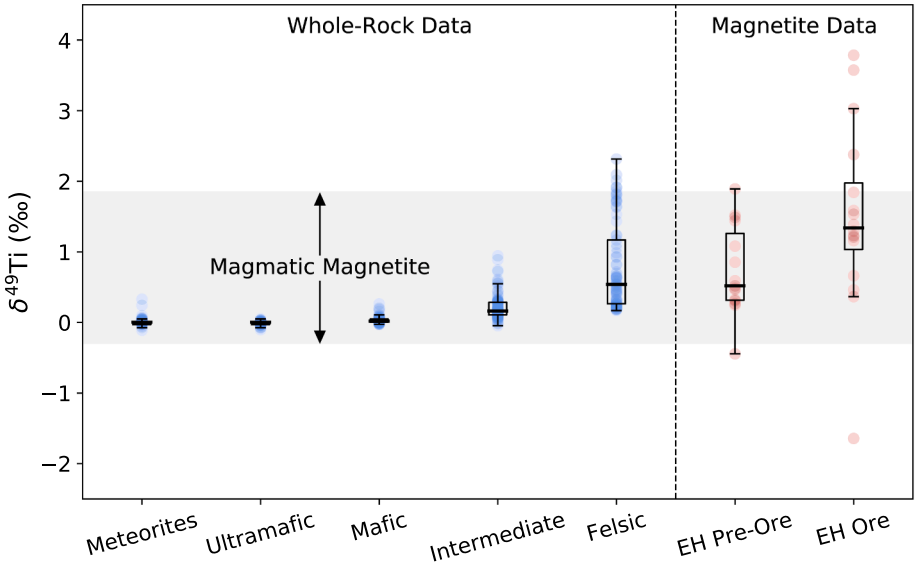

Fig. 1. Plot of whole rock and magnetite δ^{49}Ti values from published literature. Blue circles represent whole rock data, whereas red circles represent data from magnetite separates. The gray bar represents the range of magnetite compositions expected to occur in natural igneous rocks using the melt-oxide fractionation equation derived by Johnson et al. (2019) and the compositional range of natural igneous rocks; see Fig. S1. Whole rock data sourced from Millet et al. (2016), Greber et al. (2017a,b, 2021), Johnson et al. (2019, 2023), Deng et al. (2019), Hoare et al. (2020), Zhao et al. (2020), and Klaver et al. (2024). Magnetite data are from Emproto et al. (2022). The labels "EH Pre-Ore" and "EH Ore" distinguish paragenetic modes of magnetite that formed prior to and during Cu-Au mineralization, respectively.

However, these systems are incomparable to hydrothermal mineral deposits, where ligand-rich ore fluids are distinctly capable of moving vast quantities of metals (Kesler, 2005). Additionally, the discovery of the new mineral trebiskyite ($Na_3Mg_2[TiV_9O_{28}] \cdot 22H_2O$) in a post-mining secondary mineral assemblage at the Pickett Corral mine in Colorado indicates that Ti may even be mobile at room temperature and pressure conditions in certain geologic environments (Olds et al., 2024).

Previous investigations demonstrate that Ti solubility increases substantially in the presence of F-, Cl-, and solute-rich fluids (Rapp et al., 2010). Ore-forming fluids could potentially fractionate Ti isotopes if there are coordination or bonding environment changes between the mineral and solute complex. Even if mobility is poor, transport and fractionation on the sub-centimeter scale could be preserved in mineral separates. In the hydrothermal Ernest Henry iron oxide copper gold (IOCG) deposit, a 6‰ range was recorded among magnetite solely from the ore mineralization assemblage, whereas magnetite from the pre-ore assemblages exhibited δ^{49}Ti values within the range of terrestrial igneous rocks (Emproto et al., 2022). The Ernest Henry magnetite δ^{49}Ti data demonstrate that Ti isotope fractionation can occur in hydrothermal systems associated with mineralization of economic interest and highlighted the need for further experimental work to constrain fluid-mineral interaction as a viable mechanism to explain Ti isotope variation in mineral deposits (Fig. 1). In this contribution, we explore this proposed fractionation mechanism through a combination of theory and experiment.

Equilibrium mass-dependent Ti isotope fractionation is a product of differences in the vibrational frequencies of bonds to Ti atoms between two phases (Bigeleisen and Mayer, 1947; Urey, 1947). More detailed information about the terms and equations of isotopic fractionation theory can be found in e.g., Chacko et al. (2001), Schauble (2004), Liu et al. (2010), Dauphas and Schauble (2016), Blanchard et al. (2017), and others. Equilibrium Ti isotope fractionation can be described by a simple equilibrium isotope exchange reaction between two Ti-bearing substances:

$$^{47}TiA + {}^{49}TiB \leftrightharpoons {}^{49}TiA + {}^{47}TiB \quad (1)$$

where A and B represent different bonding environments. The isotope fractionation factor ($\alpha_{TiA\text{-}Ti}$) between the two Ti substances (TiA and TiB) is described by:

$$\alpha_{TiA-TiB} = \beta_{TiA}/\beta_{TiB} \quad (2)$$

Based on the Bigeleisen-Mayer equation, the reduced partition function ratios (β) correlate well with the vibrational frequencies of TiA and TiB. The general equation for β is defined as follows (Bigeleisen and Mayer, 1947; Urey, 1947):

$$\beta = \prod_{i}^{N-3} \frac{u_i^* \exp(-u_i^*/2)[1 - \exp(-u_i)]}{u_i \exp(-u_i/2)[1 - \exp(-u_i^*)]} \quad (3)$$

and

$$u_i = \frac{h\nu_i}{k_B T} \quad (4)$$

where N is the number of harmonic vibrational modes, ν_i is the vibrational frequency of the i^{th} mode, h is the Planck constant, k_B is the Boltzmann constant, and T is the temperature in Kelvin. The above expressions are applicable to predictions of equilibrium isotope fractionation behavior for different phases using first principles molecular dynamics (FPMD) simulations. From these simulations, we calculated reduced partition function ratios for a variety of aqueous Ti complexes that may exist in leaching experiments and natural systems and combine them with calculated fractionation factors from Ti-bearing minerals obtained through the same computational approach to model equilibrium fluid-mineral Ti isotope fractionation.

Metal stable isotope fractionation during acid leaching has been demonstrated for Fe isotopes (Chapman et al., 2009). Leaching of igneous rocks by acidic fluids may result in leachate that is enriched in light Fe isotopes—with δ^{56}Fe values as low as c. −1.8‰ for granite leached by HCl at 22°C under laboratory conditions (Chapman et al., 2009). Similarly, Nie et al. (2020) performed acid leaching experiments of basalts and reported that the fluid became slightly (c. –0.24 ‰ δ^{56}Fe) enriched in light Fe isotopes. These results have helped to explain observations of submarine vent fluids with reported δ^{56}Fe values of c. −0.30 to −0.77 ‰ compared to the δ^{56}Fe of typical MORB (c. 0.104 ‰) and may include influences from kinetic fractionation effects that can occur during fluid-mineral interactions (Sharma et al., 2001; Skulan et al., 2002; Dziony et al., 2014; Dauphas et al., 2017). We also performed leaching experiments of synthetic Ti-rich magnetite-ülvospinel solid solution (mgt_{50}-usp_{50}) powder under various conditions to understand how fluid-mineral Ti isotope fractionation is affected by temperature, acid type, concentration, and time, as well as to investigate non-equilibrium processes that may be represented in real data. Although Fe is significantly more mobile than Ti in most geologic fluids, the results of Emproto et al. (2022) suggest that Ti isotope fractionation occurred during Cu-Au mineralization at Ernest Henry and imply that Ti can be mobile in ore-forming fluids. As Ti isotopes appear to be resistant to some types of hydrothermal alteration and low-temperature weathering processes, observing highly fractionated Ti isotope compositions may indicate prior interaction with ligand-rich brines that could have transported elements of economic interest (Millet et al., 2016; He et al., 2022). Our experiments may therefore shed light on how Ti isotopes can be used to better understand ore formation in mineral deposits, and as an ore fertility and vectoring method. These experiments have further implications for other fluid-mediated reactions involving Ti.

2. Methods

2.1. Computational methods

We computationally determined β factors for various aqueous Ti complexes and minerals. For aqueous Ti complexes, we carried out FPMD simulations to provide configurations for calculating the final β factors. The Ti (IV) complexes selected for modeling include $[Ti(OH)_3Cl]^0$, $[Ti(OH)_3F]^0$, $[Ti(OH)_2Cl_2]^0$, $[Ti(OH)_2F_2]^0$, $[Ti(OH)Cl_3]^0$, $[Ti(OH)F_3]^0$, $[TiF_4]^0$, $[Ti(OH)_2]^{2+}$, $[Ti(OH)_4]^0$, and $[TiO(OH)_2]^0$. While not exhaustive, this array of possible coordination complexes was selected to explore a range of simple halogen (and OH) combinations that are theorized to exist in laboratory and geological environments to extract the basic mechanics of fluid-mineral Ti isotope fractionation; other complexes that are not likely to exist in geologic fluids (such as $[TiF_4]^0$) were included to acquire a more complete understanding of how bond lengths and coordination with O in water are affected by different combinations of halogens and OH (Comba and Merbach, 1987; Ryzhenko et al., 2006). This technique has been used to predict Li, Si, Mg, and Sn isotopic fractionation factors (among others) between various minerals and aqueous species (Kowalski and Jahn, 2011; Dupuis et al., 2015; Pinilla et al., 2015; Wang et al., 2019; Gao and Liu, 2021; Sun et al., 2022, 2024).

The initial structures of the relevant Ti complexes were preliminarily constructed using GaussianView software and then optimized using the DFT method (B3LYP/aug-cc-pVDZ basis set) in Gaussian software. For each simulation, the optimized Ti complex molecule is positioned at the center of a box, while the remaining 50 water molecules are randomly distributed within the box. The simulations of all Ti complexes were carried out in the NVT (canonical ensemble) thermodynamic ensemble at a fixed temperature of 300 K using a plane wave energy cut-off set at 600 eV and a 1×1×1 k-point grid. For $[Ti(OH)_2]^{2+}$, two Br atoms are added to maintain charge balance. These cell parameters are selected to guarantee that the statistical pressure is verging on zero and the densities are nearly 1 g/cm^3. The time step for the simulations of $Ti(OH)_2F_2$, $Ti(OH)Cl_3$, TiF_4, and $Ti(OH)_4$ was set to 1 fs with a total simulation time

of 50 ps. The time step for simulations of $Ti(OH)_3Cl$, $Ti(OH)_3F$, $Ti(OH)_2Cl_2$, $Ti(OH)F_3$, $[Ti(OH)_2]^{2+}$, and $TiO(OH)_2$ was set to 0.5 fs with a total simulation time of 50 ps; FPMD simulations for these coordination complexes were carried out using VASP software. The Ti-bearing solute molecule and 50 water molecules are embedded in a cubic box. Isotope fractionation has previously been shown to be a relatively local effect, and fractionations are closely linked to the local structures of the atoms of interest (e.g., Liu and Tossell, 2005; Li and Liu, 2011; Fujii and Albarede, 2018). The local structures of ions in solutions are sufficiently simulated using a solute molecule surrounded by 50 water molecules (e.g., Wang et al., 2019; Gao and Liu, 2021). Because the structure after the FPMD simulation has at least three layers of water molecules surrounding the Ti-bearing solute, each water molecule is in a location that allows for the formation of two or more hydrogen bonds. These hydrogen bonds link water molecules to form many four-, five-, and six-member rings (e.g., Xantheas and Dunning, 1993; Estrin, 1996; Ludwig et al., 1999; Liu and Tossell, 2005). The configuration disorder of the aqueous solution necessitates sampling enough configurations to acquire a converged β value. Here, we take five configurations for each aqueous coordination complex. The atomic positions of the configurations are optimized with a force convergence criterion of 1×10^{-3} eV/Å. Finally, the vibrational frequencies are calculated to predict the β values for each aqueous species.

The β factors for minerals are calculated similarly to those of the solute complexes and can be represented as:

$$\beta = \left[\prod_{i}^{N}\prod_{q}\frac{u^{*}_{q,i}\exp(-u^{*}_{i}/2)[1-\exp(-u_i)]}{u_{q,i}\exp(-u_i/2)[1-\exp(-u^{*}_{i})]}\right]^{1/Nq} \quad (5)$$

where N_q depicts the number of $\boldsymbol{q}$-vectors in the Brillouin zone. In this study, the vibrational frequencies of minerals are achieved by computing supercells. Three translational modes with vibrational frequencies verging on zero are neglected.

We utilized the same theoretical methods that we employed for calculating aqueous Ti complexes to compute the normalized partition coefficients of Ti-bearing crystalline phases including geikielite, Ti oxide (α-$Ti_2^{3+}O_3$), and hypothetical Ti-doped compositions of orthopyroxene ($Mg_{16}Ti^{3+}Si_{15}AlO_{48}$), pyrope ($Mg_{12}Al_7Ti^{4+}Si_{11}AlO_{48}$), olivine ($Mg_{32}Si_{15}Ti^{4+}O_{64}$), and clinopyroxene ($Mg_7Ti^{3+}Ca_8Si_{15}AlO_{48}$). The structure for Ti oxide was obtained from Aarons et al. (2021) and the structural data for other minerals are sourced from Wang et al. (2020), including orthopyroxene (opx), clinopyroxene (cpx), pyrope, geikielite, and olivine. Olivine with Ti^{4+} exchanged for Si^{4+} was used because experimental data indicate that this is more energetically favorable than Ti^{4+} substitution for Fe^{2+}/Mg^{2+} (Berry et al., 2007). An orthopyroxene with a similar Ti^{4+} for Si^{4+} substitution was utilized from Wang et al. (2020). Although terrestrial Ti is tetravalent, a structure for clinopyroxene exchanged with Ti^{3+} was used because this phase has Ti in 6-fold coordination, which is the most abundant CN of Ti in pyroxene group minerals on Earth (Bloise et al., 2011).

2.2. Empirical methods

Leaching samples were sourced from a structurally and chemically characterized synthetic magnetite-ülvospinel solid solution (mgt_{50}-usp_{50}) powder synthesized and characterized by the Lindsley research group at Stony Brook University. The sample was additionally measured for its Ti isotope composition using the methodology of Mathur et al. (2022). Leaching experiments were run as combinations of the following independent variables: temperature (25 or 40 °C), time (20, 200, or 1440 min with some 40- and 480-minute aliquots), acid type (HCl or HF), and acid normality (0.5 or 1N) for 28 unique experimental combinations. Approximately 50 mg of powdered sample was placed in a Teflon vial containing 10 ml of acid heated to the desired temperature on a hot plate, representing time zero. Each time step represents a unique replicate sample subjected to the same temperature and acid conditions. The yield was calculated by comparing the Ti concentration in a split of each aliquot determined by inductively coupled plasma optical emission spectrometry (ICP-OES) to the Ti concentration in solution expected from dissolving all 50 mg of sample. The remaining sample solution was dried over a hot plate, and the resulting salts were digested in 4 ml of ultrapure aqua regia (3:1 ratio of 10 M HCl to 15.2 M HNO_3) at 80 °C. This solution was dried once more before redissolving the new salts in 6 M HCl. This process ensured no precipitates were loaded onto the columns.

Column chemical separations for Ti isotope analyses were completed at Juniata College using the methodology of Mathur et al. (2022). See the Supplemental Information or Mathur et al. (2022) for further details. Purified sample solutions were analyzed for their Ti isotope abundances using multi-collector inductively coupled plasma mass spectrometry (MC-ICP-MS) on a Neptune MC-ICP-MS instrument at Rutgers University. The instrumentation configuration for Ti was identical to that of Zhu et al. (2002) with mass bias correction via standard-sample bracketing. The Origins Laboratory Ti (OL-Ti) standard used for bracketing in this study was graciously provided to us by N. Dauphas at the University of Chicago (Zhang et al., 2011; Greber et al., 2021). The 2σ error for the methodology of Mathur et al. (2022) was determined to be ±0.14‰ via multiple analyses of a synthetic solid Fe-Ti oxide standard.

3. Results

3.1. Structures and β factors of Ti-bearing aqueous species

The structures of aqueous Ti-bearing species are not set as solids, but rather in an equilibrium state of flux. To assess the structural properties of all aqueous Ti species, partial radial distribution functions (RDFs) of the Ti-O (or Ti-Cl/F) atom pair were calculated; these can be expressed as:

$$g_{Ti-O}(\mathrm{r}) = \frac{N_t}{\rho N_{Ti} N_O}\langle\sum_{i=1}^{N_{Ti}}\sum_{j=1}^{N_o}\delta(\vec{\mathrm{r}} - \vec{R}_i^{Ti} + \vec{R}_j^{O})\rangle \quad (6)$$

where ρ is the atomic number density, and the total number of atoms is denoted by N_t. The symbols N_{Ti} and N_O represent the number of Ti and O atoms, respectively. $\vec{R}$ represents atomic coordinates. The CNs for O surrounding Ti and the RDFs of various aqueous Ti species are shown in Fig. S2. For $[Ti(OH)_4]^0$, $[Ti(OH)_3F]^0$, $[Ti(OH)_2F_2]^0$, $[Ti(OH)F_3]^0$, $[TiF_4]^0$, $[Ti(OH)_3Cl]^0$, $[Ti(OH)_2Cl_2]^0$, $[Ti(OH)Cl_3]^0$, $[Ti(OH)_2]^{2+}$, $[TiO(OH)_2]^0$ and peaks for Ti-O RDF values are found at approximately 1.83 Å, 1.85 Å, 1.69 Å, 2.13 Å, 1.87 Å, 1.83 Å, 1.79 Å, 1.81 Å, 1.83 Å, and 1.87 Å, respectively (Fig. S2a). The CNs for O in each complex were approximately 4, 4, 3, 3, 2, 4, 3, 2, 5, and 5, respectively (Fig. S2b). The distance trajectory and structure snapshots are included in the supplemental information as Fig. S4–8. Note that the cumulative average of the five configurations for each complex is taken as the final 1000lnβ value. According to our calculations, the fluctuations in 1000lnβ values among the five configurations are very small (< 0.1‰) (Fig. S3). These results are consistent with investigations of aqueous Br^+ done by Gao and Liu (2021).

For the initial structure, the CN (Ti-O) of $[Ti(OH)_3Cl]^0$ in the first solvation shell is c. 3; however, as the simulation progressed over time, the CN (Ti-O) increased to 4, indicating that a water molecule is complexed with Ti and interacts with it in the range of 2.0–2.5 Å (Fig. S4a). The distance trajectories between Ti and O of the water molecules are shown in Fig. S4a and the configurations of $[Ti(OH)_3Cl]^0$ at 0 ps, 30 ps, and 50 ps are shown in Figs. S4b, S4c, and S4d, respectively. The structural changes to the complexes and distance trajectories of Ti-OH_2 (Fig. S4a–d) indicate that only one water molecule can be stably coordinated with Ti, forming the $[Ti(OH)_3Cl(H_2O)]^0$ structure (Fig. S4d).

For $[Ti(OH)_3F]^0$ in solution, after 50 ps of FPMD runtime (Fig. S4e),

the CN of Ti-O in the first solvation shell increased from c. 3 in the initial structure (Fig. S4f) to c. 4 (Figs. S4g, h), indicating the binding of a water molecule to Ti; the water molecule interacts with Ti within a radius of c. 2.0–2.5 Å (Fig. S4e). Figs. S4f, S4g, and S4h depict the structure of $[Ti(OH)_3F]^0$ in solution at 0 ps, 20 ps, and 50 ps, respectively, and Fig. S4e depicts the distance trajectory between the Ti and OH_2 atoms. The structural changes of the complexes and distance trajectories of Ti-O (Figs. S4e–h) show that the distance between Ti and OH_2 gradually shortened from the initial c. 2.5 to c. 2.1 Å, and one water molecule can be stably coordinated with Ti, forming the $[Ti(OH)_3F(H_2O)]^0$ structure (Fig. S4h).

For $[Ti(OH)_2Cl_2]^0$ in solution, after 50 ps of FPMD runtime (Figs. S5a–d), the CN of Ti-O in the first solvation shell increased from c. 2 in the initial structure (Fig. S5b) to c. 3 (Figs. S4c, d), indicating that a water molecule coordinated with Ti (Ti-OH_2) and interacted with it until the end of the simulation (Fig. S5d). Figs. S5b, S5c, and S5d depict the structure of $[Ti(OH)_2Cl_2]^0$ in solution at 0 ps, 20 ps, and 50 ps, respectively, and Fig. S5a depicts the distance trajectory between the Ti and Cl atoms. With the structural changes observed in the complexes and distance trajectories of Ti-Cl (Fig. S5a–d), as an H_2O molecule became bound to Ti (Ti-OH_2), one H atom was lost (from the H_2O) and one Cl atom gradually moved away from Ti (with the distance increasing from the initial c. 2.08 Å to as high as c. 5 Å), forming the $[Ti(OH)_3Cl]^0$ structure (Fig. S5d).

For $[Ti(OH)_2F_2]^0$ in solution, after 50 ps of FPMD runtime (Figs. S5e–h), the CN of Ti-O in the first solvation shell increased from c. 2 in the initial structure (Fig. S5f) to c. 3 (Figs. S5g, h), indicating that a water molecule coordinated with Ti (Ti-OH_2) and interacted with it in the range of c. 2.0–2.3 Å (Fig. S5e). Figs. S5f–h depict the structure of $[Ti(OH)_2F_2]^0$ in solution at 0 ps, 20 ps, and 50 ps, respectively, and Fig. S5e depicts the distance trajectory between Ti and OH_2. According to the structural changes of the complexes and distance trajectories of Ti-OH_2 (Fig. S5e-h), one water molecule can be stably coordinated with Ti, forming the $[Ti(OH)_2F_2(H_2O)]^0$ structure (Fig. S5h).

For $[Ti(OH)Cl_3]^0$ in solution, after 50 ps of FPMD runtime (Fig. S6a–d), the CN of Ti-O in the first solvation shell increased from c. 1 in the initial structure (Fig. S6b) to c. 2 (Figs. S6c and S6d), indicating that a water molecule coordinated with Ti (Ti-OH_2). Figs. S6b, S6c, and S6d depict the structure of $[Ti(OH)Cl_3]^0$ in solution at 0 ps, 20 ps, and 50 ps, respectively, and Fig. S6a depicts the distance trajectory between the Ti and OH_2 atoms. According to the structural changes of the complexes and distance trajectories of Ti-OH_2 (Fig. S6a–d), the distance between Ti and OH_2 gradually shortened from the initial c. 2.2 Å to c. 1.75 Å, and one water molecule can be stably coordinated with Ti, forming the $[Ti(OH)Cl_3(H_2O)]^0$ structure (Fig. S6d).

For $[Ti(OH)F_3]^0$ in solution, after 50 ps of FPMD runtime (Fig. S6e–h), the CN of Ti-O in the first solvation shell increased from c. 1 in the initial structure (Fig. S6f) to c. 3 (Figs. S6g and S6h), indicating that there are two water molecules coordinated with Ti (Ti-OH_2). Figs. S6f, S6g, and S6h depict the structure of $[Ti(OH)F_3]^0$ in solution at 0 ps, 20 ps and 50 ps, respectively, and Fig. S6e depicts the distance trajectory between the Ti and OH_2 atoms. According to the structural changes of the complexes and distance trajectories of Ti-OH_2 (Fig. S6e–h), two water molecules can be stably coordinated with Ti to form the $[Ti(OH)F_3(H_2O)_2]^0$ structure (Fig. S6h).

For $[TiF_4]^0$ in solution, after 50 ps of FPMD runtime (Fig. S7a–d), the CN of Ti-O in the first solvation shell increased from 0 in the initial structure (Fig. S7b) to c. 2 (Figs. S7c, d), indicating that there are two water molecules coordinated with Ti (Ti-OH_2). Figs. S7b, S7c, and S7d depict the structure of $[TiF_4]^0$ in solution at 0 ps, 20 ps and 50 ps, respectively, and Fig. S7a depicts the distance trajectory between the Ti and OH_2 atoms. According to the structural changes of the complexes and distance trajectories of Ti-OH_2 (Fig. S7a–d), the two water molecules interact with Ti^{4+} in the range of c. 1.8 to c. 2.0 Å and c. 2.0 to c. 2.4 Å, respectively (Fig. S7a), forming the $[TiF_4(H_2O)_2]^0$ structure (Fig. S7d).

For $[Ti(OH)_2]^{2+}$ in solution, after 50 ps of FPMD runtime (Fig. S7e–h), the CN of Ti-O in the first solvation shell increased from c. 2 in the initial structure (Fig. S7f) to c. 5 (Figs. S7g and S7h), indicating that there are three water molecules coordinated with Ti (Ti-OH_2). Figs. S7f, S7g, and S7h depict the structure of $[Ti(OH)_2]^{2+}$ in solution at 0 ps, 20 ps, and 50 ps, respectively, and Fig. S7e depicts the distance trajectory between the Ti and OH_2 atoms. Based on the structural changes of the complexes and distance trajectories of Ti-OH_2 (Fig. S7e–h), three water molecules will coordinate with Ti^{4+}, with one water molecule gradually moving away from the Ti atom at c. 11 ps, reaching a distance of c. 6 Å. Additionally, one of the water molecules binding to Ti lost a hydrogen atom, ultimately forming the $[Ti(OH)_3(H_2O)_2]^+$ structure (Fig. S7h).

For $[Ti(OH)_4]^0$ in solution, after 50 ps of FPMD runtime (Fig. S8a–c), the CN of Ti-O in the first solvation shell is c. 4, indicating that no water molecules are bound to Ti. Thus, the structure has not undergone significant changes and remains as $[Ti(OH)_4]^0$ at the end of the simulation. This is consistent with previous interpretations that aqueous $[Ti(OH)_4]^0$ retains a tetrahedral geometry (e.g., Vogel and Kilin, 2014), although theoretical results presented by van Sijl et al. (2010) suggest that octahedral inner and outer sphere coordination may be favored at elevated temperatures.

For $[TiO(OH)_2]^0$ in solution, after 50 ps of FPMD runtime (Fig. S8d–g), the CN of Ti-O in the first solvation shell increased from c. 3 in the initial structure (Fig. S8e) to c. 5 (Fig. S2b; Figs. S8f and S8g), indicating that there are two water molecules coordinated with Ti (Ti-OH_2). Fig. S8d depicts the distance trajectory between the Ti and OH_2 atoms and Figs. S8e, S8f, and S8g depict the structure of $[TiO(OH)_2]^0$ in solution at 0 ps, 30 ps, and 50 ps, respectively. The structural changes of the complexes and distance trajectories of Ti-OH_2 (Fig. S8d–g), indicate that two water molecules interact with Ti^{4+} in the ranges of c. 2.0–2.25 Å and c. 2.0–2.4 Å, respectively (Fig. S8d), forming the $[TiO(OH)_2](H_2O)_2]^0$ structure (Fig. S8g).

A summary of the inner sphere structural changes from the simulations is provided in Table 1. The simulated complexes are hereafter referred to by their final configurations to avoid misinterpretation of the results (e.g., results from modeling $[TiF_4]^0$ are presented as $[TiF_4(H_2O)_2]^0$). This is because most of the complexes changed their structures throughout the simulations. For most complexes, the local coordination did not change significantly (i.e., no changes to CN) between the 30 and 50 ps snapshots.

The calculation results show that the sequence of decreasing β values is $[Ti(OH)_4]^0$ > $[Ti(OH)_3Cl]^0$ > $[Ti(OH)_2F_2(H_2O)]^0$ > $[TiO(OH)_2(H_2O)_2]^0$ > $[Ti(OH)_3F(H_2O)]^0$ > $[Ti(OH)_3(H_2O)_2]^+$ > $[Ti(OH)F_3(H_2O)_2]^0$ > $[Ti(OH)_3Cl(H_2O)]^0$ > $[TiF_4(H_2O)_2]^0$ > $[Ti(OH)Cl_3(H_2O)]^0$ (Fig. 2). Among these aqueous Ti species, the β value of $[Ti(OH)_4]^0$ was largest ($^{49/47}$Ti: 3.52 500 °C), and the β value of $[Ti(OH)Cl_3(H_2O)]^0$ was smallest ($^{49/47}$Ti: 2.55 500 °C). The computed polynomial fit parameters for the β values of the aqueous Ti species are given in Table 2, and the 1000lnβ values of Ti-bearing complexes under different temperature conditions are listed in Table S1. Variations of 1000lnβ values with

Table 1
Initial and final simulated Ti coordination complex inner sphere structures and Ti CNs.

Initial Complex	Initial Ti CN	Final Complex	Final Ti CN
$[Ti(OH)_3Cl]^0$	4	$[Ti(OH)_3Cl(H_2O)]^0$	5
$[Ti(OH)_3F]^0$	4	$[Ti(OH)_3F(H_2O)]^0$	5
$[Ti(OH)_2Cl_2]^0$	4	$[Ti(OH)_3Cl]^0$	4
$[Ti(OH)_2F_2]^0$	4	$[Ti(OH)_2F_2(H_2O)]^0$	5
$[Ti(OH)Cl_3]^0$	4	$[Ti(OH)Cl_3(H_2O)]^0$	5
$[Ti(OH)F_3]^0$	4	$[Ti(OH)F_3(H_2O)_2]^0$	6
$[TiF_4]^0$	4	$[TiF_4(H_2O)_2]^0$	6
$[Ti(OH)_2]^{2+}$	2	$[Ti(OH)_3(H_2O)_2]^+$	5
$[Ti(OH)_4]^0$	4	$[Ti(OH)_4]^0$	4
$[TiO(OH)_2]^0$	3	$[TiO(OH)_2(H_2O)_2]^0$	5

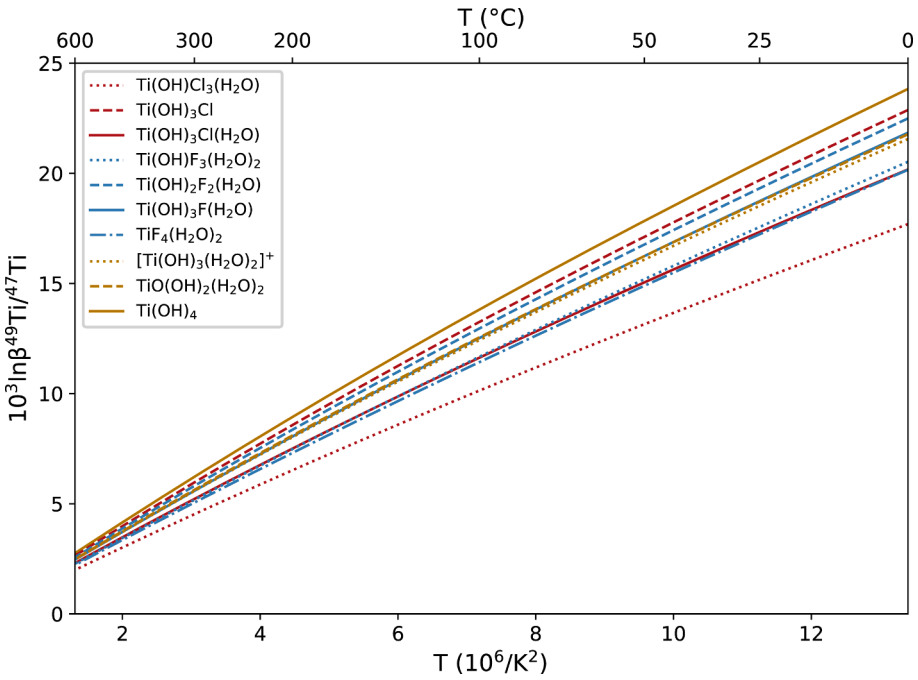

Fig. 2. Temperature dependence of 1000ln$\beta^{49}Ti/^{47}Ti$ values for the coordination complexes modeled.

Table 2
Polynomial fit parameters for the calculation of Ti isotope fractionation factors for Ti solute complexes as $1000\ln\beta = ax + bx^2 + cx^3$, where $x = 10^6/T^2$ and T is the temperature in Kelvin (273.15 K to 873.15 K).

Aqueous Ti Species	a	b	c
$[Ti(OH)_3Cl(H_2O)]^0$	1.7934 ± 0.0012	$-0.0273 \pm 1.9865 \times 10^{-4}$	$4.3363 \times 10^{-4} \pm 9.4554 \times 10^{-6}$
$[Ti(OH)_3F(H_2O)]^0$	$1.9126 \pm 9.9122 \times 10^{-4}$	$-0.0263 \pm 1.6785 \times 10^{-4}$	$3.8824 \times 10^{-4} \pm 7.9890 \times 10^{-6}$
$[Ti(OH)_3Cl]^0$	2.0575 ± 0.0013	$-0.0333 \pm 2.1914 \times 10^{-4}$	$5.3219 \times 10^{-4} \pm 1.0431 \times 10^{-5}$
$[Ti(OH)_2F_2(H_2O)]^0$	1.9978 ± 0.0014	$-0.0305 \pm 2.3702 \times 10^{-4}$	$4.9648 \times 10^{-4} \pm 1.1282 \times 10^{-5}$
$[Ti(OH)Cl_3(H_2O)]^0$	$1.5510 \pm 9.0526 \times 10^{-4}$	$-0.0219 \pm 1.5329 \times 10^{-4}$	$3.4871 \times 10^{-4} \pm 7.2962 \times 10^{-6}$
$[Ti(OH)F_3(H_2O)_2]^0$	$1.7637 \pm 7.7595 \times 10^{-4}$	$-0.0213 \pm 1.3139 \times 10^{-4}$	$2.9563 \times 10^{-4} \pm 6.2539 \times 10^{-6}$
$[TiF_4(H_2O)_2]^0$	$1.7170 \pm 6.6557 \times 10^{-4}$	$-0.0193 \pm 1.1270 \times 10^{-4}$	$2.5488 \times 10^{-4} \pm 5.3644 \times 10^{-6}$
$[Ti(OH)_3(H_2O)_2]^+$	1.91667 ± 0.00128	$-0.0292 \pm 2.1591 \times 10^{-4}$	$4.6417 \times 10^{-4} \pm 1.0277 \times 10^{-5}$
$[TiO(OH)_2(H_2O)_2]^0$	1.9349 ± 0.0012	$-0.0293 \pm 1.9772 \times 10^{-4}$	$4.5837 \times 10^{-4} \pm 9.4109 \times 10^{-6}$
$[Ti(OH)_4]^0$	2.1450 ± 0.0014	$-0.0347 \pm 2.2995 \times 10^{-4}$	$5.4668 \times 10^{-4} \pm 1.0945 \times 10^{-5}$

temperature are shown in Fig. 2.

3.2. Structures and β factors of Ti-bearing minerals

Unlike in the calculations of Ti solute geometries, our calculations for minerals did not record significant structural changes. The mineral 1000lnβ values are given in Table 3. Our computed 1000ln$\beta^{49}Ti/^{47}Ti$ values are roughly consistent with those published by Wang et al. (2020) for identical structures of Ti-doped clinopyroxene, orthopyroxene, and pyrope despite the different computational methods employed in each respective study (Fig. 3). Our calculated 1000lnβ values for olivine and opx are nearly identical to those calculated by Wang et al. (2020) (Fig. 3). However, the 1000lnβ values for pyrope and cpx are slightly smaller than those calculated by Wang et al. (2020). This is due to the different computational methods used. Wang et al. (2020) employed local density approximation, whereas this study utilizes the general gradient approximation with the Perdew-Burke-Ernzerhof functional. Literature 1000lnβ values are compiled in Table S2. A comparison of the cell parameters and volumes of titanium-bearing minerals that we calculated with existing experimental or computational results is given in Table S3. In addition, we calculated the vibration frequencies of all minerals as detailed in 'mineral frequencies' (https://doi.org/10.17632/98h3bvscvb.5). The frequencies for geikielite are compared with the computational results of Wang et al. (2020) and experimental results of Hirata et al. (1996) in Table S4.

Table 3
Polynomial fit parameters for the calculation of Ti isotope fractionation factors in minerals as $1000\ln\beta = ax + bx^2 + cx^3$, where $x = 10^6/T^2$ and T is the temperature in Kelvin (273.15 K to 873.15 K).

Crystalline Phase	a	b	c	Ti CN
giekielite	1.367	-1.165×10^{-2}	1.341×10^{-4}	6
Ti oxide	8.267×10^{-1}	-3.388×10^{-3}	1.978×10^{-5}	6
pyrope	1.5651	-1.595×10^{-2}	2.160×10^{-4}	6
clinopyroxene	1.219	-9.070×10^{-3}	6.639×10^{-4}	6
orthopyroxene	2.285	-3.801×10^{-2}	6.639×10^{-4}	4
olivine	2.358	-3.830×10^{-2}	6.395×10^{-4}	4

3.3. Leaching results

The leaching experiments were successful in inducing measurable fluid-mineral Ti isotope fractionation under laboratory conditions. The mineral leaching results are shown in Fig. 4 and data are given in Table S5. In general, longer reaction times resulted in higher yields due to increased sample dissolution under otherwise identical experimental conditions. The mgt_{50}-usp_{50} used in our experiments was measured for its Ti isotopic composition twice, yielding $\delta^{49}Ti$ values of –0.61 ‰ (±0.14 ‰) and –0.71 ‰ (±0.14 ‰), respectively (Table S5). Isotopic

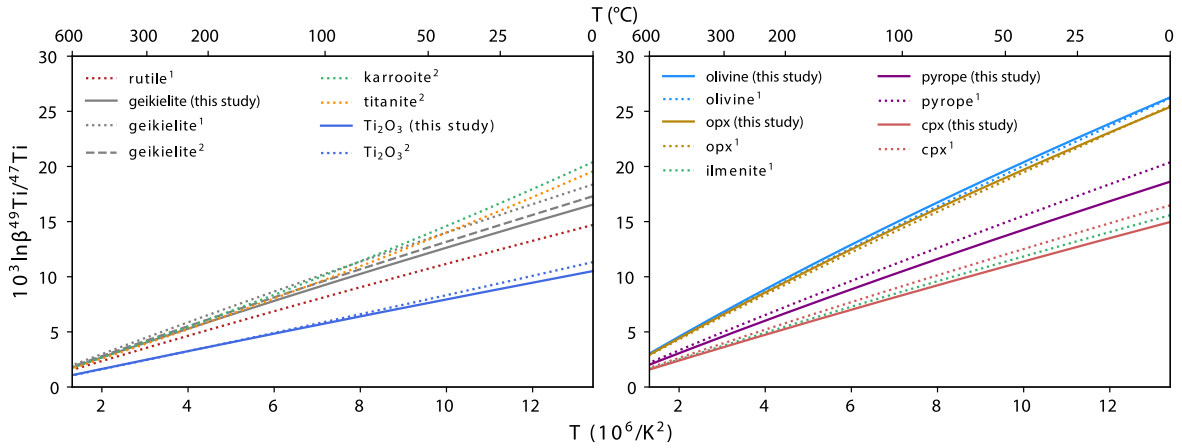

Fig. 3. Plot of $10^3 \ln\beta$ values as a function of temperature for crystalline phases. Some $10^3 \ln\beta$ values from [1]Wang et al. (2020) and [2]Aarons et al. (2021) computed using different methodologies are shown for comparison. The full list of literature $10^3 \ln\beta$ values is given in Table S2.

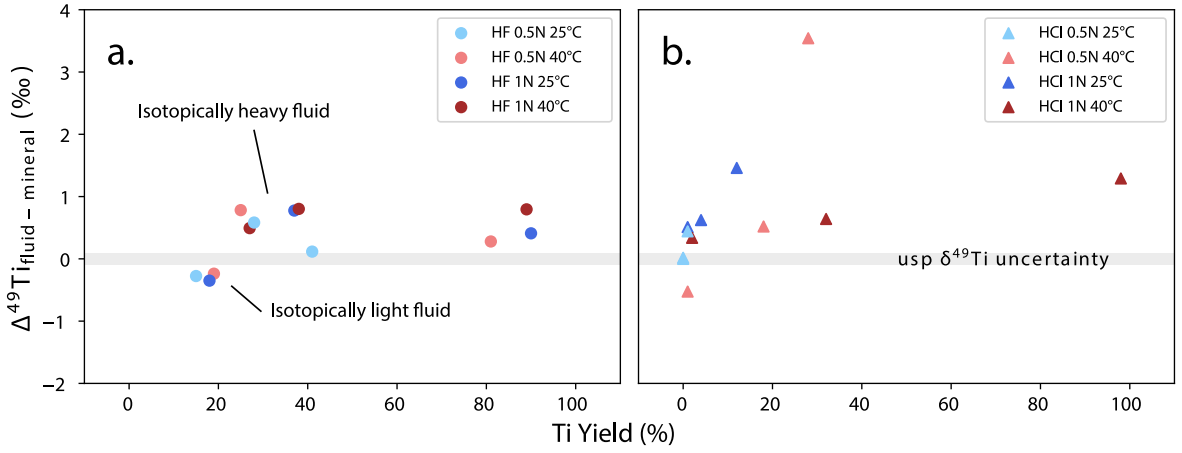

Fig. 4. Measured Ti isotope compositions for various leaching conditions using (a) HF and (b) HCl. The gray bar represents the overlap in 2σ error (±0.14 ‰) for the two measurements of the starting material. Note that multiple data for the same measurement conditions represent different time steps of parallel experiments where an aliquot was taken for isotope measurement.

analyses of the leachates indicate that, except for experiments with lower Ti yields, the fluid became isotopically heavier relative to the composition of the starting material (Fig. 4). In the HF leaching experiments, it was observed that the fluid phase became isotopically lighter relative to the starting material in the experiments with the lowest Ti yields. Only one sample from the HCl leaching experiments exhibited light Ti isotope enrichment relative to the starting material, although this sample also had a comparatively low yield (c. 0.67 %). The HF experiments produced more consistent fractionation of c. 0.6‰, whereas the magnitude of fractionation observed in the HCl experiments was less consistent. The yields were also generally higher for the HF experiments than for those that used HCl.

4. Discussion

4.1. Ti Bonding Environments in Fluids

Bond length, ligands, and CN are considered important factors influencing isotope fractionation and thus, understanding the influence of different halogen and OH combinations is useful for rationalizing differences in fractionation behaviors for different fluids (e.g., Schauble, 2004, 2007). In general, higher CNs are associated with longer bond lengths, whereas complexes with smaller CNs generally have stronger, stiffer bonds. The stronger bonding environments of complexes with small CNs leads to their enrichment in heavy isotopes, and vice versa for complexes with larger CNs. For aqueous Ti-OH-Cl species in solution, the greater the number of Cl atoms bound to Ti, the longer the average bond length of the complex—and the smaller its $1000 \ln\beta$ value. This results in a greater enrichment of lighter Ti isotopes for Cl-rich complexes, which conforms to the rule that the shorter the bond length, the greater the tendency for the phase to become enriched in heavy isotopes (e.g., Méheut and Schauble, 2014; Liu et al., 2018; Huang et al., 2019). However, for a hypothetical equilibrium fractionation scenario between $[Ti(OH)_3Cl(H_2O)]^0$ (CN = 5) and $[Ti(OH)_3Cl]^0$ (CN = 4)—two Ti-OH-Cl complexes with the same number of Cl atoms—the results indicate that the complex with the smaller CN would become enriched in heavy Ti isotopes across the modeled temperature range. This prediction aligns with the previously established rule that smaller CNs result in the preferential enrichment of heavy isotopes (e.g., Huang et al., 2013; Li et al., 2021; Liu et al., 2021).

For aqueous Ti-OH-F species in solution, the overall trend shows that as the number of F atoms bound to Ti increases, the bond length of the complex also increases. The longer bond lengths cause a decrease in its $1000 \ln\beta$ value, and result in a greater relative enrichment of lighter Ti isotopes. However, for $[Ti(OH)_2F_2(H_2O)]^0$ and $[Ti(OH)_3F(H_2O)]^0$, even though $[Ti(OH)_2F_2(H_2O)]^0$ has a higher number of F atoms than $[Ti(OH)_3F(H_2O)]^0$ (with almost identical bond lengths), its $1000 \ln\beta$ value is higher than that of $[Ti(OH)_3F(H_2O)]^0$. This is likely due primarily to differences in the complex's structure (Figs. S5h, S6h). The strong preference of the $[Ti(OH)_4]^0$ complex for heavy Ti isotopes relative to

the other complexes modeled is explained by the tetrahedral coordination of this complex throughout the simulation. In contrast, other complexes that also started as tetrahedral formed additional bonds with one or more (H_2O) O atoms during the simulation, resulting in 5- and 6-fold coordinated complexes.

We did not gather data to empirically determine the Ti coordination complex(es) present in our leaching experiments, however, complexes that may have formed in our 0.5N HF and HCl experiments are hydrated forms of $[Ti(OH)_3F]^0$ and $[Ti(OH)_3Cl]^0$, respectively, whereas the complexes present in our 1.0N HF and HCl experiments are potentially hydrated forms of $[Ti(OH)_2F_2]^0$ and $[Ti(OH)_2Cl_2]^0$, respectively (Ryzhenko et al., 2006). Similar coordination complexes are also postulated for conditions relevant to mineral deposits (500°C and 1 kbar) (Ryzhenko et al., 2006). Of these, only $[Ti(OH)_3Cl]^0$ (obtained from an initial structure of $[Ti(OH)_2Cl_2]^0$) is represented among the final coordination complex structures presented here. The complex $[Ti(OH)_4]^0$ is relevant for rutile solubility in pure water, however, its migration in the absence of other ligands is very limited—even under hydrothermal conditions (c. 1 μm at 400–700°C and 1 kbar) (Ryzhenko et al., 2006). Similarly, Ti complexed in seawater is interpreted to be in the form of $[Ti(OH)_4]^0$ or $[TiO(OH)_2]^0$ (Turner et al., 1981, Cabaniss, 1987).

It is unclear which coordination complexes are most important for Ti mobility in hydrothermal mineral systems and under what physical and chemical conditions each complex is relevant. This uncertainty inhibits quantitative modeling of Ti isotope fractionation in these systems. Although we explored different combinations of OH, F, and Cl, other elements—such as Na—may also impact Ti mobility and complexation (Rapp et al., 2010). The purpose of our computational modeling and benchtop leaching experiments is not to derive quantitative models for natural systems, but to explore basic aspects of fluid-mineral Ti isotope fractionation from which we can infer how Ti isotope fractionation may work in real mineral systems. Significantly more research into Ti complexation and ore-forming conditions present during Ti mobilization in mineral systems is required to derive reliable fluid-mineral Ti isotope fractionation models.

4.2. Modeling fractionation among minerals, melts, and fluids

Analogous to mineral-melt systems, fluid-mineral fractionation behavior in systems at or near equilibrium can be rationalized by considering the coordination changes between the fluid and mineral phases. The solute coordination complexes that were modeled largely bonded to an additional O (H_2O) atom to attain 5-fold coordination by the end of the simulation. In minerals, essential Ti in 5-fold coordination is very rare and only found in a few minerals such as innelite, fresnoite (and its Sr analogue alfredcasparite), and some lamprophyllite group minerals. In the most abundant Ti-rich minerals (e.g., oxides, titanite), Ti is almost exclusively found in 6-fold coordination. Trace amounts of Ti may also be variably accommodated at 4-fold sites in common silicate minerals through a simple substitution of Ti^{4+} for Si^{4+}. In common minerals such as pyroxenes and olivine, substitution of Ti^{4+} as a trace element onto both 6-fold and 4-fold sites may occur (Berry et al., 2007, Bloise et al., 2011). Because heavy isotopes preferentially partition into sites with smaller CNs, Ti substitution into 4-fold sites would typically enrich the mineral in heavy isotopes whereas substitution into 6-fold sites would generally concentrate light isotopes in the mineral compared to a melt or fluid phase with predominantly 5-fold coordinated Ti (Fig. 5). It should be noted that fluid equilibration with the most abundant Ti-rich minerals (Ti-rich magnetite, ilmenite, rutile, and titanite) as well as with silicates with the most common forms of Ti substitution observed in Earth systems (e.g., pyroxenes and titanite with 6-fold Ti) should result in fluid enrichment in heavy Ti isotopes under geologically relevant conditions (i.e., $T \gg 298.15$ K), because Ti in these minerals is principally in 6-fold coordination (Fig. 6). Additional considerations for mineral leaching in natural rocks are surface area (i.e., grain size), reactivity, and Ti abundance in each phase. These results suggest that the mineralogy of a rock exerts a strong influence on the Ti isotope composition of a fluid leaching Ti from it. With the above considerations, an important insight is that equilibrium fluid-mineral interaction can be projected to generally enrich the fluid in heavy Ti isotopes due to the predominance of 6-fold Ti in most rocks. This broad interpretation is supported by our computational modeling, leaching experiments, and investigations of Ti isotopes during chemical weathering by He et al. (2022) and Aarons et al. (2023).

Although we could not obtain robust fractionation factors for

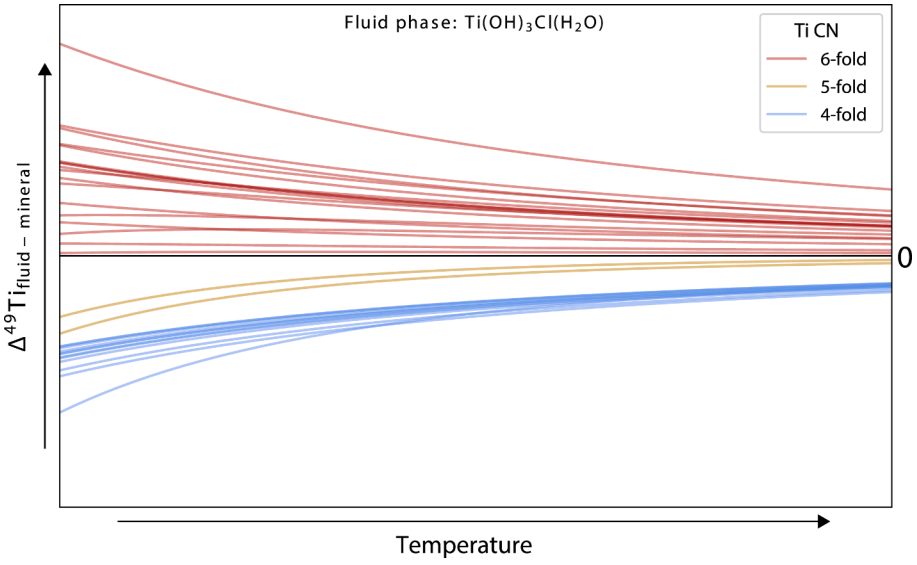

Fig. 5. Conceptual diagram showing $\Delta^{49}Ti_{fluid\text{-}mineral}$ relationships with temperature for the fluid phase $[Ti(OH)_3Cl(H_2O)]^0$ and solid phases with published polynomial expansion coefficients for the calculation of $1000ln\beta^{49}Ti/^{47}Ti$ values from Wang et al. (2020) and Aarons et al. (2021); literature data are compiled in Table S2. Line colors correspond to the CN of Ti in each phase (red: 6-fold; yellow: 5-fold; blue: 4-fold); Ti in the fluid phase is in 5-fold coordination. Because the literature $1000ln\beta^{49}Ti/^{47}Ti$ values were calculated with a different methodology, quantification could introduce systematic errors. Therefore, axis scales are not shown.

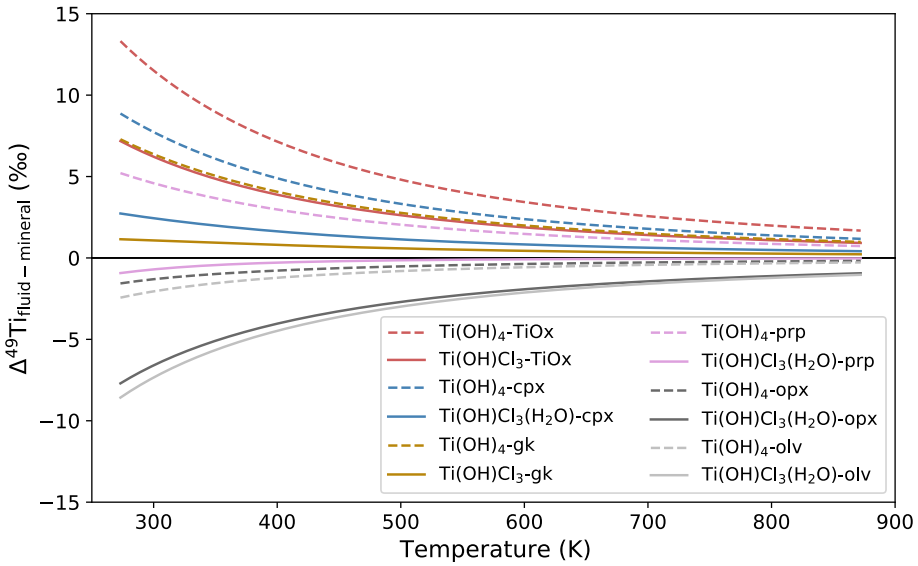

Fig. 6. Calculated $\Delta^{49}Ti_{fluid\text{-}mineral}$ relationships with temperature for the two fluids bounding the range of 1000lnβ^{49}Ti/^{47}Ti values ([Ti(OH)$_4$]^0; dashed lines and [Ti(OH)Cl$_3$H$_2$O]^0; solid lines) with the Ti phases modeled in this study. Phases with 6-coordinated Ti are plotted in color and phases with 4-coordinated Ti are in gray. Abbreviations: TiOx: α-Ti_2O_3;; cpx: Ti-doped clinopyroxene ($Mg_{15}Ti^{3+}Ca_{16}Si_{31}AlO_{96}$); gk: geikielite; prp: pyrope (low-Ti pyrope exchanged Al + Si ↔ Ti + Al); opx: Ti-doped orthopyroxene ($Mg_{16}Ti^{4+}Si_{15}O_{48}$); olv: olivine (low-Ti olivine exchanged Si ↔ Ti).

magnetite using the computational methodology we employed for the fluid complexes, general fractionation principles for a fluid-magnetite system can still be demonstrated with approximated fractionation factors. At high temperatures, the reduced partition function ratio is effectively approximated using only the first term of the expanded polynomial and can be simplified for ^{49}Ti-^{47}Ti isotope fractionation to the following:

$$1000ln\beta^{49}Ti/^{47}Ti \cong 3815F/T^2 \quad (7)$$

where F is the force constant in N/m and T is the temperature in Kelvin. See Aarons et al. (2021) and Dauphas et al. (2012, 2014) for more details on this approximation. Aarons et al. (2021) utilized a Ti-bearing magnetite force constant of 296 N/m based on Ti-O bond distances, whereas Greber et al. (2021) estimated a force constant of 365 N/m based on Ti isotope measurements of mineral separates. As mineral-fluid interactions typically occur at sub-magmatic temperatures, the above approximation introduces a significant degree of uncertainty into our calculations. Thus, our calculations as they pertain to magnetite should not be considered a reliable numerical prediction and should be revisited when more accurate derivations of the 1000lnβ^{49}Ti/^{47}Ti of magnetite (and ülvospinel) are available. For essentially all fluid composition and temperature conditions, the fluid will become enriched in heavy Ti isotopes during fluid-mineral interaction (Fig. 7). This general result aligns with the leaching results suggesting that the fluid phase will become enriched in heavy Ti isotopes during leaching. Due to

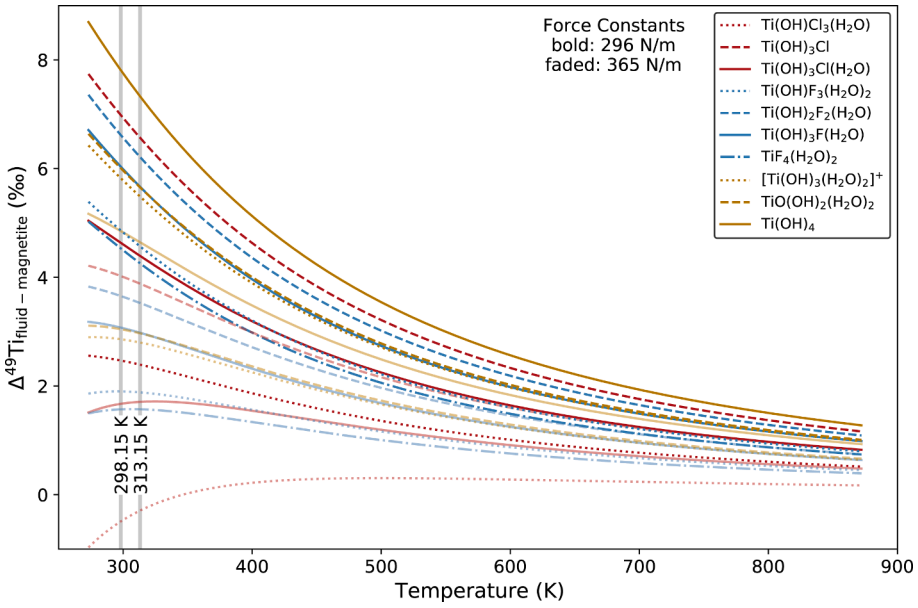

Fig. 7. Calculated $\Delta^{49}Ti_{fluid\text{-}mineral}$ relationships with temperature for all modeled fluid complexes equilibrated with Ti-bearing magnetite. Fractionation lines are colored to better convey chemistry: those with F are blue, those with Cl are red, and those without Cl or F are yellow. Bold lines utilize a force constant of 296 N/m in the calculation of the magnetite fractionation factor, whereas faded lines utilize a force constant of 365 N/m (Aarons et al., 2021, Greber et al., 2021). Gray lines demarcate the temperatures of two sets of leaching experiments.

the high degree of uncertainty surrounding this approximation, a direct numerical comparison between the empirical leaching results and modeled fluid-magnetite fractionation plotted in Fig. 7 should be avoided.

In addition to uncertainties introduced from approximating a fractionation factor for magnetite using a force constant, the calculated $1000\ln\beta^{49}Ti/^{47}Ti$ values are applicable to systems in isotopic equilibrium. Without isotopic equilibration, the leaching data are not expected to be adequately described by our computed equilibrium fractionation model. It is unlikely that any of our bench top leaching experiments achieved complete isotopic equilibrium. We will first discuss the experiments that had higher yields and resulted in an isotopically heavy fluid and then discuss the low-yield experiments that produced an isotopically light fluid. The high yields (often greater than 20 %) obtained in relatively short periods of time ($\leq$ 1 day) indicate that a substantial portion of the sample was rapidly dissolved. The acid and magnetite likely did not isotopically equilibrate in this short time span and, as a result, the Ti isotope composition of the fluid would be very similar to that of the dissolved material. A strong driving force in the dissolution reaction would be expected to diminish the extent of isotope fractionation between the reactants because mass transfer is primarily unidirectional (i.e., little to no mass is transferred back from the fluid to the mineral) under these circumstances (Pearce et al., 2012). During chemical equilibration, fluid exchange with mineral surfaces will allow the system to approach isotopic equilibration between the fluid and mineral surface. Future studies could build upon these results by chemically equilibrating minerals with fluid under various pressure and temperature conditions relevant to geologic systems (for example, using a piston cylinder apparatus).

Highly limited fluid-mineral chemical equilibration may explain the similarly small degree of Ti isotope fractionation observed in the strongly weathered basalts analyzed by He et al. (2022). However, it is worth noting that the $\Delta^{49}Ti_{fluid\text{-}residue}$ of c. 0.2‰ determined by He et al. (2022) for intense lateritic weathering is greater than zero (i.e., the fluid would be isotopically heavy), which is qualitatively consistent with our computational and experimental results that also indicate an isotopically heavy fluid during fluid-mineral interaction with most Earth materials. Similarly, Aarons et al. (2023) found that heavy Ti isotopes are preferentially incorporated into secondary minerals formed during intense chemical weathering in soils.

Even if equilibrium was assumed in laboratory experiments, there may be complications in directly applying our computational results to our experimental data. Firstly, the experimental conditions are at the edge of the temperature range for which our computed fluid $1000\ln\beta^{49}Ti/^{47}Ti$ values are calibrated. Additionally, the first-order approximations of the magnetite fractionation factor derived from estimated force constants primarily pertain to the first term of the reduced partition function ratio (see Aarons et al., 2021). Because T^2 is in the denominator in calculations of $1000\ln\beta^{49}Ti/^{47}Ti$ values, the additional terms of the reduced partition function ratios and their uncertainties become increasingly important at low temperatures. Mineral $1000\ln\beta^{49}Ti/^{47}Ti$ values are also interpreted to vary with Ti concentration, complicating the application of calculated $1000\ln\beta^{49}Ti/^{47}Ti$ values to real data (Hoare et al., 2020; Wang et al., 2020). Finally, equilibrium fractionation may not completely describe Ti isotope exchange in systems of interest, including within an experimental setup.

Kinetic isotope effects are important during water–rock interactions, especially at low temperatures (Rouxel et al., 2003; Li et al., 2021). With respect to Ti stable isotope systematics, the higher zero-point energy of bonds with ^{47}Ti compared to those with ^{49}Ti results in more easily broken bonds between ^{47}Ti and atoms in its coordination sphere. The observation of isotopically light fluid in our low-yield experiments is therefore consistent with kinetic effects. The kinetic isotope effect likely dominates isotope exchange in experiments where the fluid becomes isotopically light and may continue to detract from the extent of equilibrium fractionation observed during higher-yield experiments that made more progress towards chemical and isotopic equilibration.

While interaction with minerals could potentially fractionate Ti isotopes, some fractionation may also occur at the point of origin in magmatic-hydrothermal systems during volatile exsolution. These interactions cannot be generalized across all melt and fluid compositions. It is unknown exactly which Ti coordination complexes would be present during magma volatile exsolution in natural systems, although speciation is known to be important in other transition metal stable isotope systems, such as Fe (Schauble et al., 2001). Aarons et al. (2021) attempted to model approximated $1000\ln\beta^{49}Ti/^{47}Ti$ values for hypothetical melt compositions to understand Ti isotope fractionation differences between calc-alkaline and tholeiitic melts. We apply their approximated force constants to investigate Ti isotope fractionation induced by melt-fluid separation as a potential mechanism for modifying mineral Ti isotope compositions.

While this estimation is subjective, we apply it here as a conceptual demonstration. Computed $\Delta^{49}Ti_{fluid\text{-}melt}$ fractionation lines for hypothetical mafic (< 52 wt% SiO_2), intermediate (52–63 wt% SiO_2), and felsic (> 63 wt% SiO_2) melts equilibrating with fluids where Ti complexes as $Ti(OH)_4$ or $Ti(OH)Cl_3(H_2O)$ are plotted in Fig. 8. The complexes $Ti(OH)_4$ and $Ti(OH)Cl_3(H_2O)$ used in Fig. 8 were selected to cover the range of $1000\ln\beta^{49}Ti/^{47}Ti$ values computed for the various Ti coordination complexes.

The results of this exercise indicate that (for a given coordination complex) the higher the melt SiO_2 at the point of fluid exsolution, the lighter the fluid phase $\delta^{49}Ti$ will be. In other words, a felsic melt would theoretically exsolve an isotopically lighter fluid (with respect to Ti) than an intermediate or mafic melt. This trend could be obfuscated or even reversed if the coordination complex differs between melt compositions. Many of the coordination compounds that were modeled took on 5-fold coordination by forming an additional bond with an H_2O O atom over the course of the simulation. The melt Ti coordination for intermediate melts is assumed to be entirely 5-fold in the above model, meaning that there is likely very little change in the Ti bonding environment between the melt and fluid (and thus, very little isotope fractionation). However, most Ti-rich minerals have Ti in 6-fold coordination and will thus deplete the melt or fluid in light Ti isotopes when they precipitate. Because fluid-melt fractionation would occur at high temperatures, this process would likely result in smaller degrees of Ti isotope fractionation than equilibrium fluid-mineral interaction at sub-magmatic temperatures. For a felsic melt, the effects of melt-fluid and fluid-mineral fractionation could be additive, producing very isotopically light minerals.

To summarize, under the right conditions, fluids may be agents of significant Ti isotope fractionation effects. At magmatic temperatures, melt-fluid segregation could potentially result in fractionation of c. ±0.4‰, depending on melt and fluid compositions. At sub-magmatic temperatures, fractionation during hydrothermal mineral precipitation may be an order of magnitude larger. Equilibrium fluid-mineral interaction would generally result in an isotopically heavy fluid and an isotopically light mineral relative to the bulk Ti isotope composition of the system. During hydrothermal alteration where the mineral is instead losing Ti to the fluid, the fluid would preferentially uptake heavy Ti isotopes under equilibrium conditions. These insights have relevance to mineral systems where minerals may form from or interact with ligand-rich brines capable of transporting Ti.

4.3. Implications for mineral deposit studies

The magnetite $\delta^{49}Ti$ data reported in Emproto et al. (2022) displayed Ti isotope variations for magnetite associated with Cu-Au mineralization outside of the range consistent with fractionation driven by magmatic differentiation, whereas Ti isotopic variations for pre-ore mineralization were largely within a range consistent with terrestrial igneous rocks and could represent either primary Ti isotope compositions or Ti reapportioned during metamorphism (Emproto et al., 2022). These isotopic

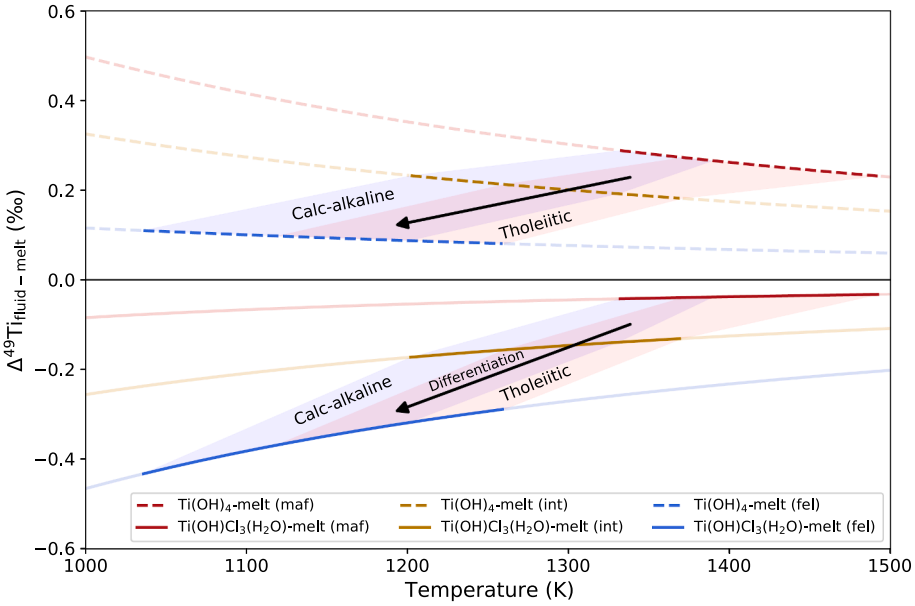

Fig. 8. Calculated $\Delta^{49}Ti_{fluid\text{-}melt}$ relationships with temperature for $Ti(OH)_4$ and $Ti(OH)Cl_3(H_2O)$ with three hypothetical "melt" compositions used to model differences in calc-alkaline and tholeiitic melt evolution by Aarons et al. (2021): mafic (maf; < 52 wt% SiO_2; 60 % 5-fold Ti, 40 % 6-fold Ti), intermediate (int; 52–63 wt % SiO_2; 100 % 5-fold Ti), and felsic (fel; > 63 wt% SiO_2; 55 % 5-fold Ti, 45 % 4-fold Ti). The calc-alkaline and tholeiitic temperature ranges are bounded by blue and red polygons, respectively. The fractionation lines are faded beyond the first and last formation temperatures of Ti-bearing minerals. Black arrows convey the $\Delta^{49}Ti_{fluid\text{-}melt}$ vs temperature trend across a hypothetical differentiation trajectory. The following approximated force constants derived in Aarons et al. (2021) were used in conjunction with Eqn. 7 to compute $1000ln\beta^{49}Ti/^{47}Ti$ values for each hypothetical melt: mafic: 423 N/m; intermediate: 468 N/m; felsic: 523 N/m.

compositions were inferred to represent initial heterogeneities in host rock composition and these ranges could be ultimately derived from magmatic oxide precipitation prior to metamorphism and alteration. However, magnetite interpreted as coeval with Cu-Au mineralization exhibited a range of c. 6‰—outside of what can be reasonably obtained through equilibrium melt-mineral fractionation. As demonstrated above, melt-fluid Ti transfer may produce some degree of Ti isotope fractionation, however, the potential fractionation is an order of magnitude smaller than equilibrium fluid-mineral fractionation. Therefore, magmatic processes do not explain the Ti isotope compositions observed at Ernest Henry.

Our results confirm the hypothesis that fluid-mineral interactions can result in measurable Ti isotope fractionation. Aqueous Ti is most stable in highly acidic/alkaline or electrolyte-rich solutions (Eremenko et al., 2001; Rapp et al., 2010). Dissolved Ca, Na, and Si have been shown to increase the solubility of Ti in aqueous fluids through poorly understood mechanisms (Manning, 2004; Rapp et al., 2010; Tanis et al., 2015, 2016; Mysen, 2019). As demonstrated during our leaching experiments, acidic fluids are capable of extracting Ti from Fe-Ti oxides and fractionating Ti isotopes in the process. This is consistent with the interpretation that the ore stage at Ernest Henry involved acidic, F-rich fluids (Schlegel et al., 2022).

While our computational and experimental results suggest that a fluid in equilibrium with Ti-bearing magnetite should deplete magnetite in heavy Ti isotopes, Ernest Henry ore stage magnetite compositions included $\delta^{49}Ti$ values that were higher than magnetite from pre-ore mineralization. Compared to other, higher temperature magnetite from occurrences such as iron oxide apatite (IOA) systems, IOCG magnetite is notably low in Ti, V, Al, Mn, and other impurities (Rodriguez-Mustafa et al., 2020). Assuming that the magnetite Ti isotope composition was not simply overprinted by total exchange with the environment, this implies that during the process of regenerative mineral replacement, pre-ore magnetite was depleted in light Ti isotopes rather than enriched in heavy Ti isotopes. The loss of light Ti isotopes (when heavy Ti isotopes are expected to be lost to the fluid under equilibrium conditions) may insinuate that the kinetic isotope effect dominates Ti isotope fractionation between the mineral and fluid during magnetite regenerative mineral replacement—and possibly during ilmenite oxyexsolution. The kinetic loss of light Ti isotopes does not explain magnetite $\delta^{49}Ti$ values below the range for magmatic magnetite, but it may drive variation to higher $\delta^{49}Ti$ values. However, diffusion during magnetite and ilmenite dissolution-reprecipitation could result in equilibrium partitioning between magnetite and ilmenite, which would result in magnetite depleted in heavy Ti isotopes and overprint any kinetic signature (Zhao et al., 2020). It bears repeating that no ilmenite exsolution lamellae were observed in any Ernest Henry magnetite—including pre-ore magnetite. Therefore, the separation of ilmenite exsolution lamellae does not entirely explain the variation in ore stage magnetite. The mechanism remains poorly understood.

In any case, our results indicate that fluid-mineral interaction may produce magnetite with Ti isotope compositions outside of the range of melt-mineral fractionation. We expect hydrothermal mineral systems to have very variable Ti isotope compositions, similar to what was observed at Ernest Henry. Observation of highly fractionated Ti isotope compositions may be a strong indicator of Ti mobility during post-magmatic processes, which may in turn be indicative of ligand-rich fluids capable of carrying significant metal endowments. Further work is necessary to understand the Ti isotope systematics of individual mineral deposits and to develop Ti isotopes as a reliable vectoring tool. Potential avenues for future research include building upon the leaching experiments by equilibrating minerals with OH–, F-, and Cl-rich fluids at temperatures and pressures relevant for geologic systems, further research into Ti complexation in mineral systems, and further investigations into Ti isotope variations in global mineral deposits.

5. Conclusions

Fluid-mineral Ti isotope fractionation is a potentially important process in modifying mineral Ti isotope compositions in systems where minerals are precipitating from or interacting with ligand-rich fluids. Combined with the available literature data, our computational results indicate that during equilibrium fluid-mineral interaction, the fluid

phase will become enriched in heavy Ti isotopes. This result is supported by our leaching experiments where powdered samples of a $mgt_{50}usp_{50}$ solid solution were leached with HCl and HF under different experimental conditions. Kinetic effects may detract from the extent of equilibrium fractionation observed in a real system and may even result in an isotopically light fluid. These results have bearing on natural mineral systems where metals were transported in ligand-rich brines and may potentially help develop a new mineral exploration tool for locating and understanding the origins of hydrothermal mineral deposits.

CRediT authorship contribution statement

Christopher Emproto: Writing – review & editing, Writing – original draft, Visualization, Investigation, Conceptualization. **Ryan Mathur:** Methodology, Investigation, Conceptualization. **Mingguang Sun:** Writing – review & editing, Writing – original draft, Visualization, Resources, Methodology, Investigation. **Adam C. Simon:** Supervision, Funding acquisition, Conceptualization. **Linda Godfrey:** Investigation.

Declaration of competing interest

The authors declare that they have no known competing financial interests or personal relationships that could have appeared to influence the work reported in this paper.

Acknowledgements

We are grateful to the Lindsley lab at Stony Brook University for kindly providing us with a well-characterized magnetite-ülvospinel solid solution sample and to N. Dauphas at the University of Chicago Origins Laboratory for donating the OL-Ti metal standard. We also thank James Roush for assistance with preliminary leaching experiments. The authors would additionally like to express their gratitude to the three anonymous reviewers for their very helpful comments. The authors also acknowledge funding for isotopic work from NSF EAR grants #2214119 and #2233425.

Appendix A. Supplementary material

The supplementary material includes a visualization of magmatic Ti isotope fractionation, distance trajectories and corresponding snapshots from FPMD simulations, a table of computed $1000\ln\beta^{49}Ti/^{47}Ti$ values at various temperatures for the coordination complexes modeled, a table of published polynomial fit parameters for the calculation of Ti isotope fractionation, comparisons of our computational results with published results, additional information on the Ti isotope column methodology, and the data table containing the leaching results plotted in Fig. 4. The supplementary material also contains files with information relevant to the mineral fractionation factor calculations. Supplementary material to this article can be found online at https://doi.org/10.1016/j.gca.2024.12.007.

Data availability

Data are available through Mendeley Data at: https://doi.org/10.17632/98h3bvscvb.5.

References

Aarons, S.M., Reimink, J.R., Greber, N.D., Heard, A.W., Zhang, Z., Dauphas, N., 2020. Titanium isotopes constrain a magmatic transition at the Hadean-Archean boundary in the Acasta Gneiss Complex. Sci. Adv. 6, eabc9959.

Aarons, S.M., Dauphas, N., Blanchard, M., Zeng, H., Nie, N.X., Johnson, A.C., Greber, N. D., Hopp, T., 2021. Clues from ab initio calculations on titanium isotopic fractionation in tholeiitic and calc-alkaline magma series. ACS Earth Space Chem. 5, 2466–2480.

Aarons, S.M., Dauphas, N., Greber, N.D., Roskosz, M., Bouchez, J., Carley, T., Liu, X.M., Rudnick, R.L., Gaillardet, J., 2023. Titanium transport and isotopic fractionation in the Critical Zone. Geochim. Cosmochim. Acta 352, 175–193.

Berry, A.J., Walker, A.M., Hermann, J., O'Neill, H., St, C., Foran, G.J., Gale, J.D., 2007. Titanium substitution mechanisms in forsterite. Chem. Geol. 242, 176–186.

Bigeleisen, J., Mayer, M.G., 1947. Calculation of equilibrium constants for isotopic exchange reactions. J. Chem. Phys. 15, 261–267.

Blanchard, M., Balan, E., Schauble, E.A., 2017. Equilibrium fractionation of non-traditional isotopes: a molecular modeling perspective. Rev. Mineral. Geochem. 82, 27–63.

Bloise, A., Pingitore, V., Miriello, D., Apollaro, C., Armentano, D., Barrese, E., Oliva, A., 2011. Flux growth and characterization of Ti- and Ni-doped enstatite single crystals. J. Cryst. Growth 329, 86–91.

Cabaniss, S.E., 1987. Titrator: an interactive program for aquatic equilibrium calculations. Envir. Sci. Tech. 21, 209–210.

Chacko, T., Cole, D.R., Horita, J., 2001. Equilibrium oxygen, hydrogen and carbon isotope fractionation factors applicable to geologic systems. Rev. Mineral. Geochem. 43, 1–81.

Chapman, J.B., Weiss, D.J., Shan, Y., Lemburger, M., 2009. Iron isotope fractionation during leaching of granite and basalt by hydrochloric and oxalic acids. Geochim. Cosmochim. Acta 73, 1312–1324.

Comba, P., Merbach, A., 1987. The titanyl question revisited. Inorg. Chem. 26, 1315–1323.

Dauphas, N., Roskosz, M., Alp, E.E., Golden, D.C., Sio, C.K., Tissot, F.L.H., Hu, M.Y., Zhao, J., Gao, L., Morris, R.V., 2012. A general moment NRIXS approach to the determination of equilibrium Fe isotopic fractionation factors: Application to goethite and jarosite. Geochim. Cosmochim. Acta 94, 254–275.

Dauphas, N., Roskosz, M., Alp, E.E., Neuville, D.R., Hu, M.Y., Sio, C.K., Tissot, F.L.H., Zhao, J., Tissandier, L., Médard, E., Cordier, C., 2014. Magma redox and structural controls on iron isotope variations in Earth's mantle and crust. Earth Planet. Sc. Lett. 398, 127–140.

Dauphas, N., John, S.G., Rouxel, O., 2017. Iron isotope systematics. Rev. Mineral. Geochem. 82, 415–510.

Dauphas, N., Schauble, E.A., 2016. Mass fractionation laws, mass-independent effects, and isotopic anomalies. Annu. Rev. Earth Pl. Sc. 44, 709–783.

Deng, Z., Moynier, F., Sossi, P.A., Chaussidon, M., 2018. Bridging the depleted MORB mantle and the continental crust using titanium isotopes. Geochem. Perspect. Lett. 9, 11–15.

Deng, Z., Chaussidon, M., Savage, P., Robert, F., Pik, R., Moynier, F., 2019. Titanium isotopes as a tracer for the plume or island arc affinity of felsic rocks. P. Natl. Acad. Sci. USA 116, 1132–1135.

Dupuis, R., Benoit, M., Nardin, E., Méheut, M., 2015. Fractionation of silicon isotopes in liquids: the importance of configurational disorder. Chem. Geol. 396, 239–254.

Dziony, W., Horn, I., Lattard, D., Koepke, J., Steinhoefel, G., Schuessler, J.A., Holtz, F., 2014. In-situ Fe isotope ratio determination in Fe–Ti oxides and sulfides from drilled gabbros and basalt from the IODP Hole 1256D in the eastern equatorial Pacific. Chem. Geol. 363, 101–113.

Emproto, C., Mathur, R., Simon, A., Bindeman, I., Godfrey, L., Dhnaram, C., Lisitsin, V., 2022. Integrated O, Fe, and Ti isotopic analysis elucidates multiple metal and fluid sources for magnetite from the Ernest Henry iron oxide copper gold (IOCG) deposit, Queensland, Australia. Ore Geol. Rev. 150, 105170.

Eremenko, B.V., Bezuglaya, T.N., Savitskaya, A.N., Malysheva, M.L., Kozlov, I.S., Bogodist, L.G., 2001. Stability of aqueous dispersions of the hydrated titanium dioxide prepared by titanium tetrachloride hydrolysis. Colloid J. 63, 173–178.

Estrin, Y., 1996. Dislocation-density–related constitutive modeling, in: Krausz, A.S., Krausz, K. (Eds.), Unified Constitutive Laws of Plastic Deformation. Academic Press, New York, pp. 69–106.

Farges, F., Brown Jr, G.E., Rehr, J.J., 1996. Coordination chemistry of Ti (IV) in silicate glasses and melts: I. XAFS study of titanium coordination in oxide model compounds. Geochim. Cosmochim. Acta 60, 3023–3038.

Farges, F., Brown Jr, G.E., 1997. Coordination chemistry of titanium (IV) in silicate glasses and melts: IV. XANES studies of synthetic and natural volcanic glasses and tektites at ambient temperature and pressure. Geochim. Cosmochim. Acta 61, 1863–1870.

Fujii, T., Albarede, F., 2018. ^{109}Ag–^{107}Ag fractionation in fluids with applications to ore deposits, archeometry, and cosmochemistry. Geochim. Cosmochim. Acta 234, 37–49.

Gao, C., Liu, Y., 2021. First-principles calculations of equilibrium bromine isotope fractionations. Geochim. Cosmochim. Acta 297, 65–81.

Greber, N.D., Dauphas, N., Puchtel, I.S., Hofmann, B.A., Arndt, N.T., 2017a. Titanium stable isotopic variations in chondrites, achondrites and lunar rocks. Geochim. Cosmochim. Acta 213, 534–552.

Greber, N.D., Dauphas, N., Bekker, A., Ptáček, M.P., Bindeman, I.N., Hofmann, A., 2017b. Titanium isotopic evidence for felsic crust and plate tectonics 3.5 billion years ago. Science 357 (6357), 1271–1274.

Greber, N.D., Pettke, T., Vilela, N., Lanari, P., Dauphas, N., 2021. Titanium isotopic compositions of bulk rocks and mineral separates from the Kos magmatic suite: Insights into fractional crystallization and magma mixing processes. Chem. Geol. 578, 120303.

He, X., Ma, J., Wei, G., Wang, Z., Zhang, L., Zeng, T., Zhang, Z., 2022. Mass-dependent fractionation of titanium stable isotopes during intensive weathering of basalts. Earth Planet. Sc. Lett. 579, 117347.

Hirata, T., Ishioka, K., Kitajima, M., 1996. Vibrational Spectroscopy and X-Ray Diffraction of Perovskite Compounds $Sr_{1-x}M_xTiO_3$(M= Ca, Mg; $0 \leq x \leq 1$). J. Solid State Chem. 124, 353–359.

Hoare, L., Klaver, M., Saji, N.S., Gillies, J., Parkinson, I.J., Lissenberg, C.J., Millet, M.-A., 2020. Melt chemistry and redox conditions control titanium isotope fractionation during magmatic differentiation. Geochim. Cosmochim. Acta 282, 38–54.
Hoare, L., Klaver, M., Muir, D.D., Klemme, S., Barling, J., Parkinson, I.J., Lissenberg, C.J., Millet, M.-A., 2022. Empirical and experimental constraints on Fe-Ti oxide-melt titanium isotope fractionation factors. Geochim. Cosmochim. Acta 326, 253–272.
Huang, F., Chen, L., Wu, Z., Wang, W., 2013. First-principles calculations of equilibrium Mg isotope fractionations between garnet, clinopyroxene, orthopyroxene, and olivine: implications for Mg isotope thermometry. Earth Planet. Sc. Lett. 367, 61–70.
Huang, F., Zhou, C., Wang, W., Kang, J., Wu, Z., 2019. First-principles calculations of equilibrium Ca isotope fractionation: Implications for oldhamite formation and evolution of lunar magma ocean. Earth Planet. Sc. Lett. 510, 153–160.
Johnson, A.C., Aarons, S.M., Dauphas, N., Nie, N.X., Zeng, H., Helz, R.T., Romaniello, S. J., Anbar, A.D., 2019. Titanium isotopic fractionation in Kilauea Iki lava lake driven by oxide crystallization. Geochim. Cosmochim. Acta 264, 180–190.
Johnson, A.C., Zhang, Z.J., Dauphas, N., Rudnick, R.L., Foden, J.D., Toc, M., 2023. Redox and mineral controls on Fe and Ti isotopic fractionations during calc-alkaline magmatic differentiation. Geochim. Cosmochim. Acta 355, 1–12.
Kesler, S.E., 2005. Ore-forming fluids. Elements 1, 13–18.
Klaver, M., Yogodzinski, G., Albert, C., Camejo-Harry, M., Elburg, M., Hoernle, K., Macpherson, C., Nowell, G., Rushmer, T., Williams, H., Millet, M.A., 2024. Widespread slab melting in modern subduction zones. Earth Planet. Sci. Lett. 626, 118544.
Kowalski, P.M., Jahn, S., 2011. Prediction of equilibrium Li isotope fractionation between minerals and aqueous solutions at high P and T: An efficient ab initio approach. Geochim. Cosmochim. Acta 75, 6112–6123.
Li, X., Liu, Y., 2011. Equilibrium Se isotope fractionation parameters: a first-principles study. Earth Planet. Sc. Lett. 304, 113–120.
Li, W., Liu, X.-M., Wang, K., Koefoed, P., 2021. Lithium and potassium isotope fractionation during silicate rock dissolution: an experimental approach. Chem. Geol. 568, 120142.
Liu, S., Li, Y., Liu, J., Ju, Y., Liu, J., Yang, Z., Shi, Y., 2018. Equilibrium lithium isotope fractionation in Li-bearing minerals. Geochim. Cosmochim. Acta Acta 235, 360–375.
Liu, S., Li, Y., Liu, J., Yang, Z., Liu, J., Shi, Y., 2021. Equilibrium Cu isotope fractionation in copper minerals: a first-principles study. Chem. Geol. 564, 120060.
Liu, Y., Tossell, J.A., 2005. Ab initio molecular orbital calculations for boron isotope fractionations on boric acids and borates. Geochim. Cosmochim. Acta 69, 3995–4006.
Liu, Q., Tossell, J.A., Liu, Y., 2010. On the proper use of the Bigeleisen–Mayer equation and corrections to it in the calculation of isotopic fractionation equilibrium constants. Geochim. Cosmochim. Acta 74, 6965–6983.
Ludwig, R., Weinhold, F., Farrar, T.C., 1999. Quantum cluster equilibrium theory of liquids: molecular clusters and thermodynamics of liquid ethanol. Mol. Phys. 97, 465–477.
Manning, C., 2004. The chemistry of subduction-zone fluids. Earth Planet. Sc. Lett. 223, 1–16.
Mathur, R., Emproto, C., Simon, A.C., Godfrey, L., Knaack, C., Vervoort, J.D., 2022. A chemical separation and measuring technique for titanium isotopes for titanium ores and iron-rich minerals. Minerals 12, 644.
Méheut, M., Schauble, E.A., 2014. Silicon isotope fractionation in silicate minerals: Insights from first-principles models of phyllosilicates, albite and pyrope. Geochim. Cosmochim. Acta 134, 137–154.
Millet, M.-A., Dauphas, N., Greber, N.D., Burton, K.W., Dale, C.W., Debret, B., Macpherson, C.G., Nowell, G.M., Williams, H.M., 2016. Titanium stable isotope investigation of magmatic processes on the Earth and Moon. Earth Planet. Sc. Lett. 449, 197–205.
Mysen, B., 2019. Aqueous fluids as transport medium at high pressure and temperature: Ti^{4+} solubility, solution mechanisms, and fluid composition. Chem. Geol. 505, 57–65.
Nie, N.X., Dauphas, N., Villalon, K.L., Liu, N., Heard, A.W., Morris, R.V., Mertzman, S.A., 2020. Iron isotopic and chemical tracing of basalt alteration and hematite spherule formation in Hawaii: a prospective study for Mars. Earth Planet. Sci. Lett. 544, 116385.
Olds, T.A., Kampf, A.R., Hughes, J.M., Adams, P.M., Marty, J., 2024. Trebiskyite, the first titanium-decavanadate mineral. Can. J. Mineral. Petrol. 62, 117–132.
Pearce, C.R., Saldi, G.D., Schott, J., Oelkers, E.H., 2012. Isotopic fractionation during congruent dissolution, precipitation and at equilibrium: Evidence from Mg isotopes. Geochim. Cosmochim. Acta 92, 170–183.
Pinilla, C., Blanchard, M., Balan, E., Natarajan, S.K., Vuilleumier, R., Mauri, F., 2015. Equilibrium magnesium isotope fractionation between aqueous Mg^{2+} and carbonate minerals: insights from path integral molecular dynamics. Geochim. Cosmochim. Acta 163, 126–139.
Rapp, J.F., Klemme, S., Butler, I.B., Harley, S.L., 2010. Extremely high solubility of rutile in chloride and fluoride-bearing metamorphic fluids: an experimental investigation. Geology 38, 323–326.
Rodriguez-Mustafa, M.A., Simon, A.C., del Real, I., Thompson, J.F.H., Bilenker, L.D., Barra, F., Bindeman, I., Cadwell, D., 2020. A continuum from iron oxide copper-gold to iron oxide-apatite deposits: evidence from Fe and O stable isotopes and trace element chemistry of magnetite. Econ. Geol. 115, 1443–1459.
Rouxel, O., Dobbek, N., Ludden, J., Fouquet, Y., 2003. Iron isotope fractionation during oceanic crust alteration. Chem. Geol. 202, 155–182.
Ryzhenko, B.N., Kovalenko, N.I., Prisyagina, N.I., 2006. Titanium complexation in hydrothermal systems. Geochem. Int. 44, 879–895.
Schauble, E.A., 2004. Applying stable isotope fractionation theory to new systems. Rev. Mineral. Geochem. 55, 65–111.
Schauble, E.A., 2007. Role of nuclear volume in driving equilibrium stable isotope fractionation of mercury, thallium, and other very heavy elements. Geochim. Cosmochim. Acta 71, 2170–2189.
Schauble, E.A., Rossman, G.R., Taylor, H.P., 2001. Theoretical estimates of equilibrium Fe-isotope fractionations from vibrational spectroscopy. Geochim. Cosmochim. Acta 65, 2487–2497.
Schlegel, T.U., Birchall, R., Shelton, T.D., Austin, J.R., 2022. Mapping the mineral zonation at the Ernest Henry iron oxide copper-gold deposit: Vectoring to Cu-Au mineralization using modal mineralogy. Econ. Geol. 117 (2), 485–494.
Sharma, M., Polizzotto, M., Anbar, A.D., 2001. Iron isotopes in hot springs along the Juan de Fuca Ridge. Earth Planet. Sc. Lett. 194, 39–51.
Skulan, J.L., Beard, B.L., Johnson, C.M., 2002. Kinetic and equilibrium Fe isotope fractionation between aqueous Fe (III) and hematite. Geochim. Cosmochim. Acta 66, 2995–3015.
Sun, M., Mathur, R., Chen, Y., Yuan, S., Wang, J., 2022. First-principles study on equilibrium Sn isotope fractionations in hydrothermal fluids. Acta Geol. Sin.-English 96 (6), 2125–2134.
Sun, M., Mathur, R., Gao, C., Chen, Y., Yuan, S., 2024. Equilibrium Sn isotope fractionation between aqueous Sn and Sn-bearing minerals: Constrained by first-principles calculations. Am. Mineral. 109 (2), 265–273.
Tanis, E.A., Simon, A., Tschauner, O., Chow, P., Xiao, Y., Burnley, P., Cline, C.J., Hanchar, J.M., Pettke, T., Shen, G., Zhao, Y., 2015. The mobility of Nb in rutile-saturated NaCl- and NaF-bearing aqueous fluids from 1–6.5 GPa and 300–800°C. Am. Mineral. 100, 1600–1609.
Tanis, E.A., Simon, A., Zhang, Y., Chow, P., Xiao, Y., Hanchar, J.M., Tschauner, O., Shen, G., 2016. Rutile solubility in NaF–NaCl–KCl-bearing aqueous fluids at 0.5–2.79 GPa and 250–650°C. Geochim. Cosmochim. Acta 177, 170–181.
Turner, D.R., Whitfield, M., Dickson, A.G., 1981. The equilibrium speciation of dissolved components in freshwater and sea water at 25°C and 1 atm pressure. Geochim. Cosmochim. Acta 45, 855–881.
Urey, H.C., 1947. The thermodynamic properties of isotopic substances. J. Chem. Soc. (resumed) 562–581.
Van Baalen, M.R., 1993. Titanium mobility in metamorphic systems: a review. Chem. Geol. 110, 233–249.
van Sijl, J., Allan, N.L., Davies, G.R., van Westrenen, W., 2010. Titanium in subduction zone fluids: First insights from ab initio molecular metadynamics simulations. Geochim. Cosmochim. Acta 74, 2797–2810.
Vogel, D.J., Kilin, D.S., 2014. Electron Dynamics of Solvated $Ti(OH)_4$. MRS Proceedings 1647.
Wang, W., Zhou, C., Liu, Y., Wu, Z., Huang, F., 2019. Equilibrium Mg isotope fractionation among aqueous Mg^{2+}, carbonates, brucite and lizardite: Insights from first-principles molecular dynamics simulations. Geochim. Cosmochim. Acta 250, 117–129.
Wang, W., Huang, S., Huang, F., Zhao, X., Wu, Z., 2020. Equilibrium inter-mineral titanium isotope fractionation: implication for high-temperature titanium isotope geochemistry. Geochim. Cosmochim. Acta 269, 540–553.
Xantheas, S.S., Dunning, T.H., 1993. Ab initio studies of cyclic water clusters $(H_2O)_n$, n=1–6. I. Optimal structures and vibrational spectra. J. Chem. Phys. 99, 8774–8792.
Zhang, J., Dauphas, N., Davis, A.M., Pourmand, A., 2011. A new method for MC-ICPMS measurement of titanium isotopic composition: Identification of correlated isotope anomalies in meteorites. J. Anal. Atom. Spectrom. 26, 2197.
Zhao, X., Tang, S., Li, J., Wang, H., Helz, R., Marsh, B., Zhu, X., Zhang, H., 2020. Titanium isotopic fractionation during magmatic differentiation. Contrib. Mineral. Petr. 175.
Zhu, X.K., Makishima, A., Guo, Y., Belshaw, N.S., O'Nions, R.K., 2002. High precision measurement of titanium isotope ratios by plasma source mass spectrometry. Int. J. Mass Spectrom. 220, 21–29.